MISSOURI S&T

Missouri University of Science and Technology

Scholars' Mine

Electrical and Computer Engineering Faculty Research & Creative Works

Electrical and Computer Engineering

01 Jan 1995

Analysis of a Current-Regulated Brushless DC Drive

Keith Corzine
Missouri University of Science and Technology

S. D. Sudhoff

H. J. Hegner

Follow this and additional works at: https://scholarsmine.mst.edu/ele_comeng_facwork

Part of the Electrical and Computer Engineering Commons

Recommended Citation

ANALYSIS OF A CURRENT-REGULATED BRUSHLESS DC DRIVE

K. A. Corzine, Student Member S. D. Sudhoff, Member
School of Electrical Engineering
University of Missouri - Rolla
Rolla, Missouri 65401

H. J. Hegner, Member
Naval Surface Warfare Center
Annapolis Detachment, Carderock Division
Annapolis, Maryland 21402

Abstract - Current-regulated brushless dc machines are used in a wide variety of applications including robotics, actuators, electric vehicles, and recently, ship propulsion systems. When conducting system analysis of this or any other type of drive, average-value reduced-order models are invaluable since they provide a means of rapidly predicting the electromechanical dynamics and are readily linearized for control system synthesis. In this paper, a highly accurate average-value reduced-order model of a hysteresis current-regulated brushless dc drive is set fourth. In so doing, it is demonstrated that the drive exhibits five distinct operating modes. The physical cause of each of these modes is explained and a mathematical model for each mode is set fourth. The mathematical models are verified both experimentally and through the use of computer simulation. It has been found that the model set fourth herein is on the order of 300 times faster than a detailed computer simulation in calculating electromechanical transients.

I. INTRODUCTION

Current-regulated brushless dc machines are used in many applications including robotics, actuators, electric vehicles, and ship propulsion. This drive system offers high efficiency since there are no field losses as well as nearly ideal torque control at low-to-moderate speeds. At high speeds, performance degrades as the current regulation becomes less effective due to an increase in the machine back emf.

For the purposes of control design and analysis, both average-value models (in which the inverter switching is represented on an average value basis) and reduced-order models (in which stator dynamics are neglected) [1] of drive systems are invaluable tools. Such models can be used to rapidly determine the electromechanical behavior of the system or linearized for the purpose of applying linear system theory.

In [2-3], the performance of a current-regulated brushless dc system is discussed based on studies using an experimental drive system and a detailed simulation, respectively. Herein, an average-value reduced-order model of a hysteresis current regulated surface-mounted permanent-magnet drive is set fourth. This model

can be used to rapidly predict the steady-state and transient performance of this drive, and is also linearizable for control system synthesis.

In developing a model for a current-regulated brushless dc drive, it will be shown that the drive exhibits five distinct operating modes. In Mode 1, which applies at low speeds, the reference currents are tracked. In this case, the drive may be modeled by assuming that the actual currents are equal to the reference currents. However, as the rotor speed is increased, the hysteresis current control is unable to continuously track the reference current because of the increased back emf. Modes 2-5 represent various degrees of this effect, each of which exhibits its own characteristic current waveforms.

In this paper, an explanation and analysis of each of these operating modes is set fourth. The predictions of the resulting model compare well with results obtained experimentally and using a computer simulation.

II. SYSTEM DESCRIPTION

Fig 1. illustrates a current-regulated voltage-source brushless dc drive system. In addition to the machine and inverter, the system includes a supervisory current control and a hysteresis current control. The supervisory control calculates the commanded currents, i^*_{abcs}, such that if the actual currents are equal to the commanded currents the electromagnetic torque is equal to the commanded torque, T^*_e. The hysteresis current control compares the commanded currents to the actual currents of the machine, i_{abcs}, and switches the inverter transistors in such a way that the commanded currents are obtained.
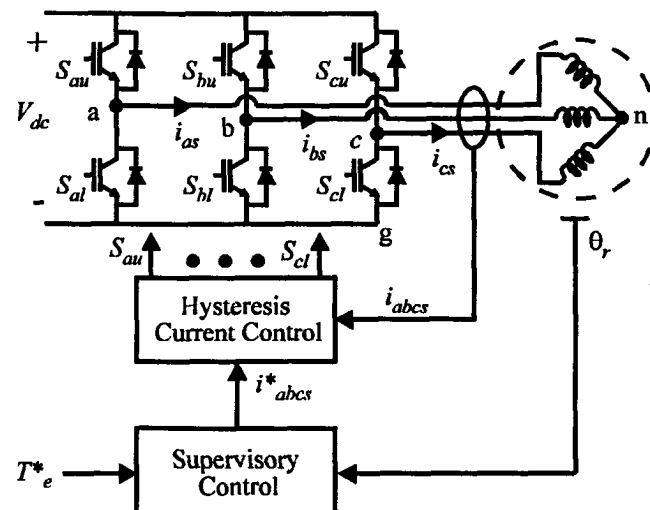

Figure 1. Current-regulated brushless dc machine drive.

A. Permanent-Magnet Synchronous Machine

A 2-pole, 3-phase permanent-magnet synchronous machine is shown in Fig. 2. Therein, each lumped winding actually represents a sinusoidally distributed winding. The mechanical rotor position and speed are denoted θ_{rm} and ω_{rm}, respectively. The electrical rotor position and speed, θ_r and ω_r, are $P/2$ times the corresponding mechanical quantities, where P is the number of poles. Assuming the machine to be of the surface-mounted magnet type, to have a sinusoidal back emf, that the effects of magnetic saturation of the stator iron as well as eddy currents are negligible, and that machine is wye-connected the voltage equations of the permanent-magnet synchronous machine are given by [4]

$$v_{as} = r_s i_{as} + L_{ss}\frac{di_{as}}{dt} + \omega_r \lambda_m' \cos(\theta_r) \tag{1}$$

$$v_{bs} = r_s i_{bs} + L_{ss}\frac{di_{bs}}{dt} + \omega_r \lambda_m' \cos(\theta_r - \frac{2\pi}{3}) \tag{2}$$

$$v_{cs} = r_s i_{cs} + L_{ss}\frac{di_{cs}}{dt} + \omega_r \lambda_m' \cos(\theta_r + \frac{2\pi}{3}) \tag{3}$$

where r_s, L_{ss}, and λ_m' denote the stator resistance, stator self inductance (the leakage inductance plus 3/2 times the magnetizing inductance), and the flux linkage due to the permanent magnet, respectively. For the purposes of developing an analytical model of the drive system, it is convenient to express the machine equations in terms of q- and d-axis variables. This transformation between abc and qd variables may be expressed

$$f_{qd0s}^r = K_s^r f_{abcs} \tag{4}$$

where

$$K_s^r = \frac{2}{3}\begin{bmatrix} \cos(\theta_r) & \cos\left(\theta_r - \frac{2\pi}{3}\right) & \cos\left(\theta_r + \frac{2\pi}{3}\right) \\ \sin(\theta_r) & \sin\left(\theta_r - \frac{2\pi}{3}\right) & \sin\left(\theta_r + \frac{2\pi}{3}\right) \\ \frac{1}{2} & \frac{1}{2} & \frac{1}{2} \end{bmatrix} \tag{5}$$
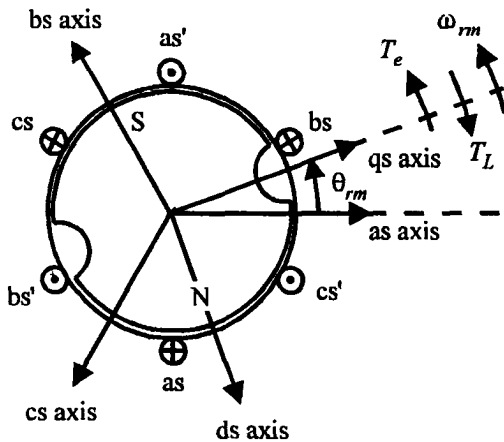

Figure 2. Permanent-magnet synchronous machine.

and

$$f_{abcs} = [\ f_{as}\ \ f_{bs}\ \ f_{cs}\ ]^T \tag{6}$$

$$f_{qd0s}^r = [\ f_{qs}^r\ \ f_{ds}^r\ \ f_{0s}^r\ ]^T. \tag{7}$$

In (4-7), f may be a voltage, current, or flux linkage. Transforming the voltage equations to the rotor reference frame yields

$$v_{qs}^r = r_s i_{qs}^r + \omega_r L_{ss} i_{ds}^r + \omega_r \lambda_m' + L_{ss}\frac{di_{qs}^r}{dt} \tag{8}$$

$$v_{ds}^r = r_s i_{ds}^r - \omega_r L_{ss} i_{qs}^r + L_{ss}\frac{di_{ds}^r}{dt}. \tag{9}$$

Since the machine is wye-connected, all zero sequence variables are zero and thus the zero sequence voltage equation is not listed above. It can be shown that in terms of qd variables [4]

$$T_e = \frac{3}{2}\frac{P}{2}\lambda_m' i_{qs}^r. \tag{10}$$

Although this machine model cannot be applied to every permanent magnet synchronous machine, it is sufficient for many drive systems. In the event that a more detailed machine model is required, the reader is referred to [5].

B. Inverter Drive

The inverter consists of six switching devices, whose gate signals are denoted S_{xy} where 'x' represents phase and may be 'a', 'b', or 'c', and y denotes the position and is either 'u' if the valve is in the upper half of the bridge or 'l' if the valve is in the lower half. The dc supply voltage to the inverter is denoted V_{dc} and is assumed to be constant. From (1-3), the zero sequence voltage must be zero. Therefore, the machine's phase-to-neutral voltages are related to the inverter phase-to-ground voltages by

$$v_{as} = \frac{2}{3}v_{ag} - \frac{1}{3}v_{bg} - \frac{1}{3}v_{cg} \tag{11}$$

$$v_{bs} = \frac{2}{3}v_{bg} - \frac{1}{3}v_{ag} - \frac{1}{3}v_{cg} \tag{12}$$

$$v_{cs} = \frac{2}{3}v_{cg} - \frac{1}{3}v_{ag} - \frac{1}{3}v_{bg}. \tag{13}$$

C. Hysteresis Current Control

The hysteresis current control governs the switching of the six inverter valves such that the actual currents i_{abcs} are held near the currents commanded by the supervisory control, i_{abcs}^*. Herein, the hysterisis control strategy depicted in Fig. 3. is utilized. As can be seen, there are two switching states for each leg, either S_{xu} is on and S_{xl} is off (the positive state), or S_{xu} is off and S_{xl} is on (the negative state), where x may be 'a','b', or 'c'. The parameter h denotes the hysteresis level. If $i_{xs} < i_{xs}^* - h$ and the state of the x'th leg is negative, then a state transition is made to the positive state. Conversely, if $i_{xs} > i_{xs}^* + h$ and the state of the x'th leg is positive, a transition is made to the negative state. Using this type of control with a sufficiently large V_{dc} guarantees that each actual phase current will always be within h of the corresponding commanded phase current resulting in nearly sinusoidal currents. A condition in which the a-phase current deviates from the commanded current by more than h will be referred to as loss of current tracking.
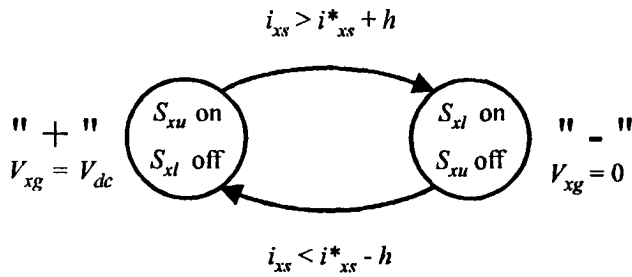
$$i_{xs} > i^*_{xs} + h$$

$$" + "$$
$$V_{xg} = V_{dc}$$

$$S_{xu} \text{ on}$$
$$S_{xl} \text{ off}$$

$$S_{xl} \text{ on}$$
$$S_{xu} \text{ off}$$

$$" - "$$
$$V_{xg} = 0$$

$$i_{xs} < i^*_{xs} - h$$

Figure 3. State transition diagram for one leg
of hysteresis controlled inverter.

D. Supervisory Control

The supervisory control determines the current command i^*_{abcs} required in order to achieve the commanded torque, T^*_e. Several methods can be used to calculate i^*_{abcs}, some of which employ flux weakening [6]. Although the model developed herein is applicable for any supervisory control, in the studies to follow, flux weakening is not used. Regardless of the supervisory control scheme implemented, i^{r*}_{qs} and i^{r*}_{ds} are first calculated, then transformed to machine variables using

$$f_{abcs} = [K^r_s]^{-1} f^r_{qd0s}. \tag{14}$$

For the purpose of the derivations to follow, it will be convenient to define several variables which relate to the supervisory control. First, the commanded q- and d-axis voltages are defined by setting the actual currents equal to the commanded currents in (8-9) and neglecting stator dynamics which yields

$$v^{r*}_{qs} = r_s i^{r*}_{qs} + \omega_r L_{ss} i^{r*}_{ds} + \omega_r \lambda'_m \tag{15}$$

$$v^{r*}_{ds} = r_s i^{r*}_{ds} - \omega_r L_{ss} i^{r*}_{qs}. \tag{16}$$

The amplitude and phase of the commanded voltages may be expressed

$$v^*_s = \sqrt{v^{*2}_{qs} + v^{*2}_{ds}} \tag{17}$$

$$\phi^*_v = \text{angle}(v^{r*}_{qs} - j v^{r*}_{ds}) \tag{18}$$

where $j = \sqrt{-1}$. Defining

$$\hat{\theta}_r = \theta_r + \phi^*_v \tag{19}$$

allows the commanded voltages to be expressed in terms of abc variables as

$$v^*_{as} = v^*_s \cos(\hat{\theta}_r) \tag{20}$$

$$v^*_{bs} = v^*_s \cos(\hat{\theta}_r - \tfrac{2\pi}{3}) \tag{21}$$

$$v^*_{cs} = v^*_s \cos(\hat{\theta}_r + \tfrac{2\pi}{3}). \tag{22}$$

It is also convenient to express the amplitude and phase of the commanded currents as

$$i^*_s = \sqrt{\left(i^{r*}_{qs}\right)^2 + (i^{r*}_{ds})} \tag{23}$$

$$\phi^*_i = \text{angle}(i^{r*}_{qs} - j i^{r*}_{ds}). \tag{24}$$

Whereupon the abc variable current command may be expressed

$$i^*_{as} = i^*_s \cos(\hat{\theta}_r - \phi^*_v + \phi^*_i) \tag{25}$$

$$i^*_{bs} = i^*_s \cos(\hat{\theta}_r - \phi^*_v + \phi^*_i - \tfrac{2\pi}{3}) \tag{26}$$

$$i^*_{cs} = i^*_s \cos(\hat{\theta}_r - \phi^*_v + \phi^*_i + \tfrac{2\pi}{3}). \tag{27}$$

Finally, the magnitude and angle of the machine impedance are defined by

$$Z = \sqrt{r^2_s + \omega^2_r L^2_{ss}} \tag{28}$$

$$\phi_z = \text{angle}(r_s + j \omega_r L_{ss}). \tag{29}$$

III. MODEL DEVELOPMENT

With the system described, an average-value reduced-order model will be developed which describes the system operation. In this model, the effect of inverter switching is represented on an average-value basis of the machine equations, and the stator electrical dynamics are also neglected [1]. In addition, it will be assumed that h is small enough that it may be considered to be zero for the purposes of describing the current waveform. It will be seen that for some operating conditions, the actual torque is equal to the commanded torque. However, for high speed or high commanded torque conditions, the dc supply voltage is not sufficient to achieve commanded currents and hence the commanded torque. The term inverter saturation will be used to describe operating conditions where commanded torque is not achieved. Five modes of system operation will be defined depending on the severity of inverter saturation. The first four modes will be analyzed to determine the average q- and d-axis current as well as the average dc link current. The fifth operating mode is well beyond the normal operation of the system and will not be considered. Once the average currents are known, any other variables of interest are readily calculated from machine equations.

A. Mode 1 Operation

At low speeds, the hysteresis current regulator guarantees that each of the phase currents is within h of the commanded current. Since the actual currents are tracking the reference currents, the average q- and d-axis currents are equal to the commanded q- and d-axis currents

$$\bar{i}^r_{qs} = i^{r*}_{qs} \tag{30}$$

$$\bar{i}^r_{ds} = i^{r*}_{ds} \tag{31}$$

where the $^-$ is used to denote average value taken over one-half cycle of the waveform. In order to calculate the average dc current into the inverter, it is convenient to first calculate the average power into the machine

$$\bar{P}_{in} = \tfrac{3}{2}(\overline{v^r_{qs} i^r_{qs}} + \overline{v^r_{ds} i^r_{ds}}). \tag{32}$$

Herein, (32) will be approximated as

$$\bar{P}_{in} = \tfrac{3}{2}(\bar{v}^r_{qs} \bar{i}^r_{qs} + \bar{v}^r_{ds} \bar{i}^r_{ds}). \tag{33}$$

The accuracy of this assumption will be verified experimentally. If the inverter losses are neglected, and the dc supply voltage changes slowly compared to switching harmonics of I_{dc}, the average dc link current may be approximated

$$\bar{I}_{dc} = \frac{\bar{P}_{in}}{V_{dc}}. \tag{34}$$

The average value current equations (30-31), and (34) have thus been established for Mode 1. They can be used to calculate $\bar{i}\,_{qs}^{r}$, $\bar{i}\,_{ds}^{r}$, and $\bar{I}_{dc}$.

It will be shown in the following section that the system does not exhibit inverter saturation for operating conditions which ensure

$$v_s^* < \frac{V_{dc}}{\sqrt{3}} \qquad (35)$$

in which case the analysis just set fourth is applicable. For operating conditions where the commanded voltage, v_s^*, exceeds this limit inverter saturation occurs.

B. Mode 2 Operation

It is not possible for an inverter to produce a line-to-line voltage greater than V_{dc}, however, it is possible, from (20), for the commanded line-to-line voltage to be greater than V_{dc}. Commanding a line-to-line voltage slightly greater than V_{dc} results in Mode 2 operation. Mode 2 operation will be analyzed by describing the a-phase current over one-half of a cycle. Alternatively, all three phase currents could be described over a 60° interval, however, the choice is arbitrary.

Fig. 4 displays an expanded view of the a-phase current during Mode 2 operation. In Fig. 4,

θ_{rd} = Angle at which i_{as} departs from i_{as}^*
    due to $v_{as}^* - v_{bs}^* > V_{dc}$
θ_{ra} = Angle at which i_{as} returns to i_{as}^*
$i_{as1}(\hat{\theta}_r) = i_{as}(\hat{\theta}_r)$ for $\theta_{rd} < \hat{\theta}_r < \theta_{ra}$
$i_{as2}(\hat{\theta}_r) = i_{as}(\hat{\theta}_r)$ for $\theta_{rd} + \frac{\pi}{3} < \hat{\theta}_r < \theta_{ra} + \frac{\pi}{3}$

The departure angle θ_{rd} is found by noting that at $\hat{\theta}_r = \theta_{rd}$

$$v_{as}^* - v_{bs}^* = V_{dc}. \qquad (36)$$

Substituting (20-21) into (36) and solving for θ_{rd} yields

$$\theta_{rd} = -\cos^{-1}\left(\frac{V_{dc}}{\sqrt{3}\,v_s^*}\right) - \frac{\pi}{6}. \qquad (37)$$
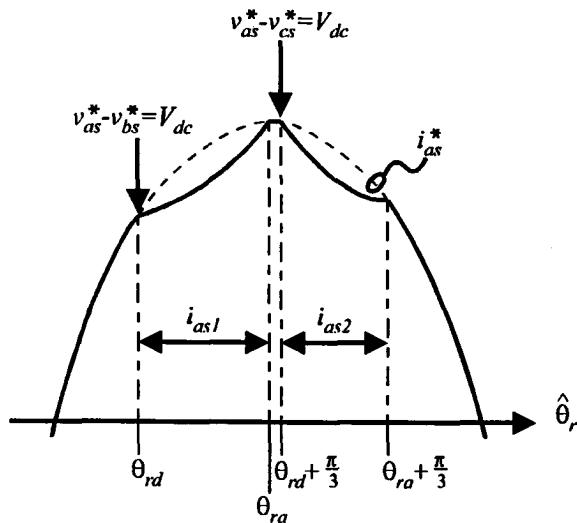

Figure 4. The a-phase current in Mode 2.

As shown by (37), the departure angle exists only if

$$v_s^* \geq \frac{V_{dc}}{\sqrt{3}}. \qquad (38)$$

Therefore, the upper limit of Mode 1 operation is defined by (38) as stated previously. After $v_{as}^* - v_{bs}^*$ becomes less than V_{dc}, i_{as} returns to its reference value. However, at $\hat{\theta}_r = \theta_{rd} + \frac{\pi}{3}$, $v_{as}^* - v_{cs}^*$ becomes greater than V_{dc} at which time the a-phase current departs again.

As illustrated in Fig. 4, for $\theta_{rd} < \hat{\theta}_r < \theta_{ra}$, the a-phase current becomes less than $i_{as}^* - h$ so the hysteresis controller commands the positive switching state. Thus,

$$v_{ag} = V_{dc}. \qquad (39)$$

Similarly, the b-phase current is greater than $i_{bs}^* + h$, therefore the hysteresis current control switches the b-phase transistors such that

$$v_{bg} = 0. \qquad (40)$$

Since the c-phase is tracking over this interval,

$$v_{cs} = v_{cs}^*. \qquad (41)$$

Using (41) and (13), v_{cg} can be found as a function of v_{cs}^*, which when combined with (39-40) and (11) yields

$$v_{as} = \tfrac{1}{2}V_{dc} - \tfrac{1}{2}v_s^* \cos(\hat{\theta}_r + \tfrac{2\pi}{3}). \qquad (42)$$

It is now possible predict the departure angle and calculate the a-phase voltage for $\theta_{rd} < \hat{\theta}_r < \theta_{ra}$. Substituting (42) into (1) and solving for the a-phase current yields

$$i_{as1}(\hat{\theta}_r) = I_{aso}e^{-\left(\frac{\hat{\theta}_r - \sigma}{\tau}\right)} + (K)\left[1 - e^{-\left(\frac{\hat{\theta}_r - \sigma}{\tau}\right)}\right]$$

$$+ \frac{A}{2Z}\left[\cos(\sigma + \alpha - \phi_z)e^{-\left(\frac{\hat{\theta}_r - \sigma}{\tau}\right)} - \cos\left(\hat{\theta}_r + \alpha - \phi_z\right)\right]$$

$$+ \frac{\omega_r \lambda_m'}{Z}\left[\cos(\sigma - \phi_v^* - \phi_z)e^{-\left(\frac{\hat{\theta}_r - \sigma}{\tau}\right)} - \cos\left(\hat{\theta}_r - \phi_v^* - \phi_z\right)\right] \qquad (43)$$

where values of A, K, α, σ, and I_{aso} are given in Table 1. From (43), i_{as} can be predicted while outside of its envelope. When this current returns to its envelope, it will again be equal to i_{as}^*. Thus, by setting (43) equal to i_{as}^* it is possible to find the arrival angle, θ_{ra} by solving

$$i_{as1}(\theta_{ra}) - i_{as}^*(\theta_{ra}) = 0. \qquad (44)$$

From Fig. 4, θ_{ra} must be between θ_{rd} and $\theta_{rd} + \frac{\pi}{3}$. A good starting point for a numerical solution is

$$\theta_{ra} = \theta_{rd} + \frac{\pi}{3}. \qquad (45)$$

Note that θ_{rd} is also a solution of (44), thus (44) should be solved with care.

Solving for $i_{as2}(\hat{\theta}_r)$ is completely analogous to the solution of $i_{as1}(\hat{\theta}_r)$, and the solution is of the same form as (43) where the coefficients are listed in Table 1, wherein the n subscript is used to denote the particular non-tracking interval.

Table 1. Current Equation Parameters for Mode 2.					
	A	K	α	σ_n	I_{aso}
$i_{as1}(\hat{\theta}_r)$	v_s^*	$1/2$	$2\pi/3$	θ_{rd}	$i_{as}^*\vert_{\sigma_1}$
$i_{as2}(\hat{\theta}_r)$	v_s^*	$1/2$	$-2\pi/3$	$\theta_{rd} + \pi/3$	$i_{as}^*\vert_{\sigma_2}$

At this point, i_{as} can be completely described over a 180° interval. In particular

$$i_{as} = \begin{cases} i_{as1}, & \theta_{rd} < \hat{\theta} < \theta_{ra} \\ i_{as}^*, & \theta_{ra} < \hat{\theta} < \theta_{rd} + \frac{\pi}{3} \\ i_{as2}, & \theta_{rd} + \frac{\pi}{3} < \hat{\theta} < \theta_{ra} + \frac{\pi}{3} \\ i_{as}^*, & \theta_{ra} < \hat{\theta} < \theta_{rd} + \pi \end{cases} \quad (46)$$

The average q-axis current may be expressed

$$\bar{i}_{qs}^r = \frac{2}{\pi} \int_{\theta_{ro}}^{\theta_{ro}+\pi} i_{as}(\hat{\theta}_r)\cos(\hat{\theta}_r - \phi_v^*)d\hat{\theta}_r \quad (47)$$

where θ_{ro} is the starting angle for integration. For the angles over which i_{as} is tracking, the integral can be evaluated symbolically which yields

$$\bar{i}_{qs,t}^r = \frac{2}{\pi}\left(\bar{i}_{qs,int}^r \big|_{\theta_{ra}+\frac{\pi}{3}}^{\theta_{rd}+\pi} + \bar{i}_{qs,int}^r \big|_{\theta_{ra}}^{\theta_{rd}+\frac{\pi}{3}}\right) \quad (48)$$

where

$$i_{qs,int}^r = \frac{i_s^*}{4}\sin(2\hat{\theta}_r - 2\phi_v^* + \phi_i^*) + \frac{i_s^*}{2}\hat{\theta}_r\cos(\phi_i^*). \quad (49)$$

When i_{as} is not tracking, the integral is difficult to evaluate symbolically and will be solved using Simpson's integration method with four integration intervals. For convenience, an integration function which approximates the integral of $s(\hat{\theta}_r)$ over an interval from θ_{r1} to θ_{r2}, is defined

$$S_{\theta_{r1}}^{\theta_{r2}}[s(\hat{\theta}_r)] = \frac{\theta_{r2}-\theta_{r1}}{12}[s(\theta_{r1}) + 4s(\frac{3}{4}\theta_{r1} + \frac{1}{4}\theta_{r2})$$
$$+ 2s(\frac{1}{2}\theta_{r1} + \frac{1}{2}\theta_{r2}) + 4s(\frac{1}{4}\theta_{r1} + \frac{3}{4}\theta_{r2}) + s(\theta_{r2})]. \quad (50)$$

Defining the function

$$s_{qn}(\hat{\theta}_r) = i_{asn}(\hat{\theta}_r)\cos(\hat{\theta}_r - \phi_v^*) \quad (51)$$

allows the component of the average q-axis current for the non-tracking intervals to be expressed

$$\bar{i}_{qs,nt}^r = \frac{2}{\pi}\left\{S_{\theta_{rd}}^{\theta_{ra}}[s_{q1}(\hat{\theta}_r)] + S_{\theta_{rd}+\frac{\pi}{3}}^{\theta_{ra}+\frac{\pi}{3}}[s_{q2}(\hat{\theta}_r)]\right\}. \quad (52)$$

The overall average q-axis current is the sum of (48) and (53), or

$$\bar{i}_{qs}^r = \bar{i}_{qs,t}^r + \bar{i}_{qs,nt}^r. \quad (53)$$

The average d-axis current may be obtained from

$$\bar{i}_{ds}^r = \frac{2}{\pi} \int_{\theta_{ro}}^{\theta_{ro}+\pi} i_{as}(\hat{\theta}_r)\sin(\hat{\theta}_r - \phi_v^*)d\hat{\theta}_r. \quad (54)$$

Repeating the procedure that was used to find the average q-axis current yields

$$\bar{i}_{ds,t}^r = \frac{2}{\pi}\left(\tilde{i}_{ds,int}^r \big|_{\theta_{ra}+\frac{\pi}{3}}^{\theta_{rd}+\pi} + \tilde{i}_{ds,int}^r \big|_{\theta_{ra}}^{\theta_{rd}+\frac{\pi}{3}}\right) \quad (55)$$

$$i_{ds,int}^r = -\frac{i_s^*}{4}\cos(2\theta_r - 2\phi_v^* + \phi_i^*) - \frac{i_s^*}{2}\hat{\theta}_r\sin(\phi_i^*) \quad (56)$$

$$\bar{i}_{ds,nt}^r = \frac{2}{\pi}\left\{S_{\theta_{rd}}^{\theta_{ra}}[s_{d1}(\hat{\theta}_r)] + S_{\theta_{rd}+\frac{\pi}{3}}^{\theta_{ra}+\frac{\pi}{3}}[s_{d2}(\hat{\theta}_r)]\right\} \quad (57)$$

$$s_{dn}(\hat{\theta}_r) = i_{asn}(\hat{\theta}_r)\sin(\hat{\theta}_r - \phi_v^*) \quad (58)$$

$$\bar{i}_{ds}^r = \bar{i}_{ds,t}^r + \bar{i}_{ds,nt}^r. \quad (59)$$

With $\bar{i}_{qs}^r$ and $\bar{i}_{ds}^r$ known, the average q- and d-axis voltages can be found from (15-16), the power into the machine can be approximated using (33), and the average dc current can be found from (34). The reduced-order model has now been established for Mode 2 operation.

There is an upper limit to Mode 2 operation. It will be demonstrated in the following section that for operating conditions for which

$$\theta_{ra} > -\cos^{-1}\left(\frac{V_{dc}}{3v_s^*}\right) + \frac{\pi}{3} \quad (60)$$

the waveforms qualitatively change, in which case drive operation exhibits a higher degree of saturation.

C. Mode 3 Operation

If v_s^* is slightly increased while in Mode 2 operation, the number of intervals over which the a-phase current no longer tracks the reference increases from 2 to 3 per half-cycle. The typical a-phase current for Mode 3 is illustrated in Fig. 5. where

$$i_{as} = \begin{cases} i_{as1}, & \theta_{rd} < \hat{\theta}_r < \theta_{rmid} \\ i_{as2}, & \theta_{rmid} < \hat{\theta}_r < \theta_{ra} \\ i_{as}^*, & \theta_{ra} < \hat{\theta}_r < \theta_{rd2} \\ i_{as3}, & \theta_{rd2} < \hat{\theta}_r < \theta_{rd} + \frac{\pi}{3} \\ i_{as4}, & \theta_{rd} + \frac{\pi}{3} < \hat{\theta}_r < \theta_{rmid} + \frac{\pi}{3} \\ i_{as5}, & \theta_{rmid} + \frac{\pi}{3} < \hat{\theta}_r < \theta_{ra} + \frac{\pi}{3} \\ i_{as}^*, & \theta_{ra} + \frac{\pi}{3} < \hat{\theta}_r < \theta_{rd2} + \frac{\pi}{3} \\ i_{as6}, & \theta_{rd2} + \frac{\pi}{3} < \hat{\theta}_r < \theta_{rd} + \frac{2\pi}{3} \\ i_{as7}, & \theta_{rd} + \frac{2\pi}{3} < \hat{\theta}_r < \theta_{rmid} + \frac{2\pi}{3} \\ i_{as}^*, & \theta_{rmid} + \frac{2\pi}{3} < \hat{\theta}_r < \theta_{rd} + \pi \end{cases} \quad (61)$$

Three departure angles are present in this mode. The first occurs at $\hat{\theta}_r = \theta_{rd}$ since the b-phase voltage, v_{bs}, is limited to $-\frac{2}{3}V_{dc}$. It can be shown from (11-13) that when this occurs, v_{as} and v_{cs} are limited to $\frac{1}{3}V_{dc}$ causing the a-phase current to depart. Therefore, the first
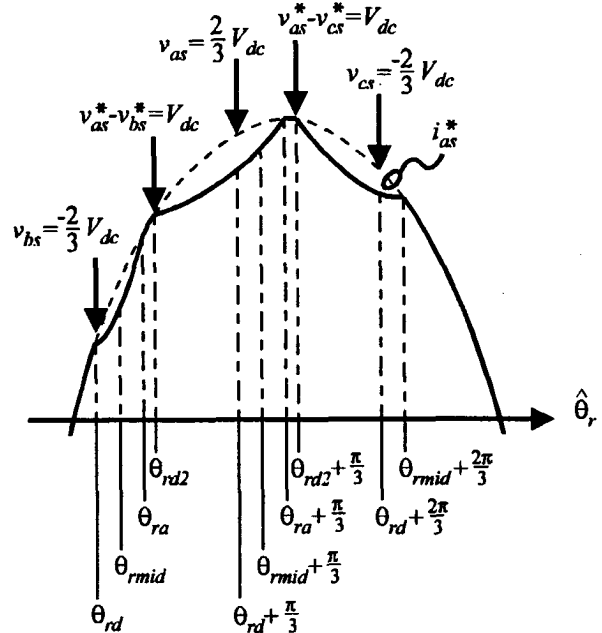

Figure 5. The a-phase current in Mode 3.

departure angle can be found by setting v_{as}^* equal to $\frac{1}{3}V_{dc}$ which yields

$$\theta_{rd} = -\cos^{-1}\left(\frac{V_{dc}}{3v_s^*}\right). \tag{62}$$

Since the waveforms exhibit symmetry over a 60° interval, v_{as} is limited to $\frac{2}{3}V_{dc}$ at $\theta_{rd} + \frac{\pi}{3}$. Therefore, in order for a system to be in Mode 2 operation, the Mode 2 arrival angle must be less than the Mode 3 departure angle plus 60° as indicated by (60).

The second departure angle, θ_{rd2}, occurs because the commanded line-to-line voltage between phases a and b exceeds V_{dc} and can be calculated from the Mode 2 departure angle equation (37).

The third occurs when the commanded line-to-line voltage v_{ac} exceeds V_{dc} and is calculated by adding 60° to θ_{rd2} as indicated in Fig. 5. The inflections within the non-tracking intervals are due to the arrivals and departures of the b- and c-phase currents.

After an analysis of the seven non-tracking intervals, similar to that presented in the previous section, it was found that the currents could be described by (43) with the coefficients given in Table 2.

Table 2. Current Equation Parameters for Mode 3.

	A	K	α	σ_n	I_{aso}
$i_{as1}(\hat{\theta}_r)$	0	1/3	0	θ_{rd}	$i_{as}^*\|_{\sigma_1}$
$i_{as2}(\hat{\theta}_r)$	v_s^*	1/2	$2\pi/3$	θ_{rmid}	$i_{as1}\|_{\sigma_2}$
$i_{as3}(\hat{\theta}_r)$	v_s^*	1/2	$2\pi/3$	θ_{rd2}	$i_{as2}\|_{\sigma_3}$
$i_{as4}(\hat{\theta}_r)$	0	2/3	0	$\theta_{rd} + \pi/3$	$i_{as3}\|_{\sigma_4}$
$i_{as5}(\hat{\theta}_r)$	v_s^*	1/2	$-2\pi/3$	$\theta_{rmid} + \pi/3$	$i_{as4}\|_{\sigma_5}$
$i_{as6}(\hat{\theta}_r)$	v_s^*	1/2	$-2\pi/3$	$\theta_{rd2} + \pi/3$	$i_{as5}\|_{\sigma_6}$
$i_{as7}(\hat{\theta}_r)$	0	1/3	0	$\theta_{rd} + 2\pi/3$	$i_{as6}\|_{\sigma_7}$

From Fig. 5, it can be seen that the midpoint and arrival angles, θ_{rmid} and θ_{ra}, can be found by numerically solving

$$i_{as7}(\theta_{rmid}) - i_{as}^*(\theta_{rmid}) = 0 \tag{63}$$

and

$$i_{as2}(\theta_{ra}) - i_{as}^*(\theta_{ra}) = 0 \tag{64}$$

respectively. Calculating $\bar{i}_{qs}^r$ and $\bar{i}_{ds}^r$ can be accomplished as with Mode 2. The resulting expressions are

$$\bar{i}_{qs,t}^r = \frac{2}{\pi}\left(\tilde{i}_{qs,int}^r\Big|_{\theta_{rmid}+\frac{2\pi}{3}}^{\theta_{rd}+\pi} + \tilde{i}_{qs,int}^r\Big|_{\theta_{ra}+\frac{\pi}{3}}^{\theta_{rd2}+\frac{\pi}{3}} + \tilde{i}_{qs,int}^r\Big|_{\theta_{ra}}^{\theta_{rd2}}\right) \tag{65}$$

$$\bar{i}_{qs,nt}^r = \frac{2}{\pi}\left\{S_{\theta_{rd}}^{\theta_{rmid}}[s_{q1}(\hat{\theta}_r)] + S_{\theta_{rmid}}^{\theta_{ra}}[s_{q2}(\hat{\theta}_r)]\right.$$
$$+ S_{\theta_{rd2}}^{\theta_{rd}+\frac{\pi}{3}}[s_{q3}(\hat{\theta}_r)] + S_{\theta_{rd}+\frac{\pi}{3}}^{\theta_{rmid}+\frac{\pi}{3}}[s_{q4}(\hat{\theta}_r)] + S_{\theta_{rmid}+\frac{\pi}{3}}^{\theta_{ra}+\frac{\pi}{3}}[s_{q5}(\hat{\theta}_r)]$$
$$\left. + S_{\theta_{rd2}+\frac{\pi}{3}}^{\theta_{rd}+\frac{2\pi}{3}}[s_{q6}(\hat{\theta}_r)] + S_{\theta_{rd}+\frac{2\pi}{3}}^{\theta_{rmid}+\frac{2\pi}{3}}[s_{q7}(\hat{\theta}_r)]\right\} \tag{66}$$

$$\bar{i}_{ds,t}^r = \frac{2}{\pi}\left(\tilde{i}_{ds,int}^r\Big|_{\theta_{rmid}+\frac{2\pi}{3}}^{\theta_{rd}+\pi} + \tilde{i}_{ds,int}^r\Big|_{\theta_{ra}+\frac{\pi}{3}}^{\theta_{rd2}+\frac{\pi}{3}} + \tilde{i}_{ds,int}^r\Big|_{\theta_{ra}}^{\theta_{rd2}}\right) \tag{67}$$

$$\bar{i}_{ds,nt}^r = \frac{2}{\pi}\left\{S_{\theta_{rd}}^{\theta_{rmid}}[s_{d1}(\hat{\theta}_r)] + S_{\theta_{rmid}}^{\theta_{ra}}[s_{d2}(\hat{\theta}_r)]\right.$$
$$+ S_{\theta_{rd2}}^{\theta_{rd}+\frac{\pi}{3}}[s_{d3}(\hat{\theta}_r)] + S_{\theta_{rd}+\frac{\pi}{3}}^{\theta_{rmid}+\frac{\pi}{3}}[s_{d4}(\hat{\theta}_r)] + S_{\theta_{rmid}+\frac{\pi}{3}}^{\theta_{ra}+\frac{\pi}{3}}[s_{d5}(\hat{\theta}_r)]$$
$$\left. + S_{\theta_{rd2}+\frac{\pi}{3}}^{\theta_{rd}+\frac{2\pi}{3}}[s_{d6}(\hat{\theta}_r)] + S_{\theta_{rd}+\frac{2\pi}{3}}^{\theta_{rmid}+\frac{2\pi}{3}}[s_{d7}(\hat{\theta}_r)]\right\} \tag{68}$$

$$\bar{i}_{qs}^r = \bar{i}_{qs,t}^r + \bar{i}_{qs,nt}^r \tag{69}$$

$$\bar{i}_{qs}^r = \bar{i}_{qs,t}^r + \bar{i}_{qs,nt}^r. \tag{70}$$

The average dc link current is approximated by (33-34).

Consider a system operating in Mode 3. As v_s^* is increased, the non-tracking intervals will become more extensive and the tracking intervals will shrink until i_{as2} joins i_{as3} and i_{as5} joins i_{as6}. When this occurs,

$$\theta_{ra} > \theta_{rd2} \tag{71}$$

and the qualitative nature of the current waveforms once again changes. In this case, inverter operation enters Mode 4.

D. Mode 4 Operation

Mode 4 operation is characterized by the a-phase current displayed in Fig. 6. where

$$i_{as} = \begin{cases} i_{as1}, & \theta_{rd} < \hat{\theta}_r < \theta_{ra} - \frac{2\pi}{3} \\ i_{as2}, & \theta_{ra} - \frac{2\pi}{3} < \hat{\theta}_r < \theta_{rd} + \frac{\pi}{3} \\ i_{as3}, & \theta_{rd} + \frac{\pi}{3} < \hat{\theta}_r < \theta_{ra} - \frac{\pi}{3} \\ i_{as4}, & \theta_{ra} - \frac{\pi}{3} < \hat{\theta}_r < \theta_{rd} + \frac{2\pi}{3} \\ i_{as5}, & \theta_{rd} + \frac{2\pi}{3} < \hat{\theta}_r < \theta_{ra} \\ i_{as}^*, & \theta_{ra} < \hat{\theta}_r < \theta_{rd} + \pi \end{cases} \tag{72}$$

The departure angle can be predicted using the equation for the first departure angle of Mode 3 (62), and the currents in the non-tracking intervals are described by (43) with the coefficients of Table 3.
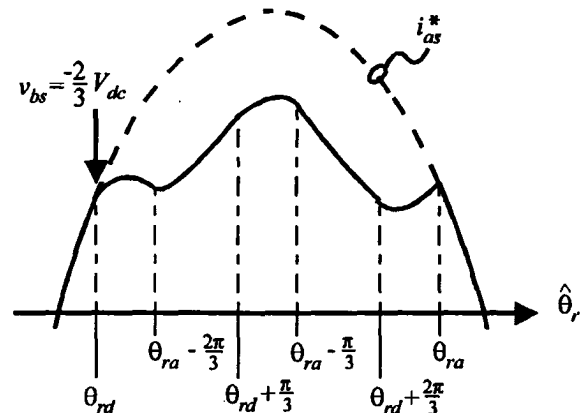

Figure 6. The a-phase current in Mode 4.

Table 3. Current Equation Parameters for Mode 4.

	A	K	α	σ_n	I_{aso}
$i_{as1}(\hat{\theta}_r)$	0	1/3	0	θ_{rd}	$i_{as}^*|_{\sigma_1}$
$i_{as2}(\hat{\theta}_r)$	v_s^*	1/2	$2\pi/3$	$\theta_{ra}-2\pi/3$	$i_{as1}|_{\sigma_2}$
$i_{as3}(\hat{\theta}_r)$	0	2/3	0	$\theta_{rd}+\pi/3$	$i_{as2}|_{\sigma_3}$
$i_{as4}(\hat{\theta}_r)$	v_s^*	1/2	$-2\pi/3$	$\theta_{ra}-\pi/3$	$i_{as3}|_{\sigma_4}$
$i_{as5}(\hat{\theta}_r)$	0	1/3	0	$\theta_{rd}+2\pi/3$	$i_{as4}|_{\sigma_5}$

The arrival angle is found by simultaneously solving

$$I_{aso2}(\theta_{ra}) = i_{as1}\left(\theta_{ra}-\tfrac{2\pi}{3}\right) \tag{73}$$

$$I_{aso3}(\theta_{ra}) = i_{as2}\left(\theta_{rd}+\tfrac{\pi}{3}\right) \tag{74}$$

$$I_{aso5}(\theta_{ra}) = I_{aso3}(\theta_{ra}) - I_{aso1} \tag{75}$$

$$i_{as5}(\theta_{ra}) - i_{as}^*(\theta_{ra}) = 0 \tag{76}$$

Using a similar procedure as was used with Mode 2, expressions for $\bar{i}_{qs}^r$ and $\bar{i}_{ds}^r$ can be obtained. In particular,

$$\bar{i}_{qs,t}^r = \tfrac{2}{\pi}\tilde{i}_{qs,t}^r|_{\theta_{ra}}^{\theta_{rd}+\pi} \tag{77}$$

$$\bar{i}_{qs,nt}^r = \tfrac{2}{\pi}\left\{S_{\theta_{rd}}^{\theta_{ra}-\frac{2\pi}{3}}[s_{q1}(\hat{\theta}_r)] + S_{\theta_{ra}-\frac{2\pi}{3}}^{\theta_{rd}+\frac{\pi}{3}}[s_{q2}(\hat{\theta}_r)] \right.$$
$$\left. +S_{\theta_{rd}+\frac{\pi}{3}}^{\theta_{ra}-\frac{\pi}{3}}[s_{q3}(\hat{\theta}_r)] + S_{\theta_{ra}-\frac{\pi}{3}}^{\theta_{rd}+\frac{2\pi}{3}}[s_{q4}(\hat{\theta}_r)] + S_{\theta_{rd}+\frac{2\pi}{3}}^{\theta_{ra}}[s_{q5}(\hat{\theta}_r)] \right\} \tag{78}$$

$$\bar{i}_{ds,t}^r = \tfrac{2}{\pi}\tilde{i}_{ds,t}^r|_{\theta_{ra}}^{\theta_{rd}+\pi} \tag{79}$$

$$\bar{i}_{ds,nt}^r = \tfrac{2}{\pi}\left\{S_{\theta_{rd}}^{\theta_{ra}-\frac{2\pi}{3}}[s_{d1}(\hat{\theta}_r)] + S_{\theta_{ra}-\frac{2\pi}{3}}^{\theta_{rd}+\frac{\pi}{3}}[s_{d2}(\hat{\theta}_r)] \right.$$
$$\left. +S_{\theta_{rd}+\frac{\pi}{3}}^{\theta_{ra}-\frac{\pi}{3}}[s_{d3}(\hat{\theta}_r)] + S_{\theta_{ra}-\frac{\pi}{3}}^{\theta_{rd}+\frac{2\pi}{3}}[s_{d4}(\hat{\theta}_r)] + S_{\theta_{rd}+\frac{2\pi}{3}}^{\theta_{ra}}[s_{d5}(\hat{\theta}_r)] \right\} \tag{80}$$

$$\bar{i}_{qs}^r = \bar{i}_{qs,t}^r + \bar{i}_{qs,nt}^r \tag{81}$$

$$\bar{i}_{ds}^r = \bar{i}_{ds,t}^r + \bar{i}_{ds,nt}^r. \tag{82}$$

The average dc link current is found from (33-34).

Increasing v_s^* from Mode 4 operation will eventually cause Mode 4 to be exceeded. This occurs when

$$\theta_{ra} - \pi > \theta_{rd} \tag{83}$$

If (83) is satisfied, the inverter reverts to six step operation. In Mode 5, the system is well beyond its normal operating range, therefore, this final mode is not considered herein.

IV. MODEL VERIFICATION

The analysis just set fourth will be verified both experimentally and using a computer simulation. The test system consists of a 4-pole, 3/4-hp machine with $r_s = 2.99\ \Omega$, $L_{ss} = 11.35$ mH, and $\lambda_m' = 0.156$ V•sec/rad. The inverter was operated at $V_{dc} = 145$ V with a hysteresis level of $h = 0.1$ A. It was observed that the IGBT and diode forward voltage drops were 1.7 and 1.0 volts respectively. The IGBT turn on and turn off times were 400 ms and 600 ms, and a deadtime of 1.5 μsec was used to avoid shoot through. Figs. 7-10 illustrate the q-axis current, d-axis current, dc current, and
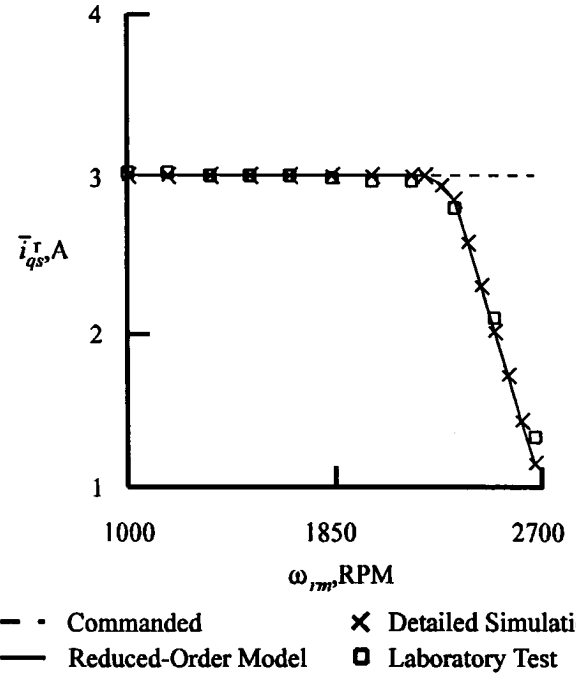

Figure 7. Average q-axis current.

electromagnetic torque versus rotor speed with $i_{qs}^{r*} = 3.0$ A and $i_{ds}^{r*} = 0$. Therein, the average q- and d-axis currents for the laboratory tests were obtained at each point by storing the a-phase current in a storage oscilloscope and then processing this online data. In order to take into account the semiconductor voltage drops, V_{dc} was reduced by 3.4 (2*1.7) volts in the reduced-order model and computer simulation.
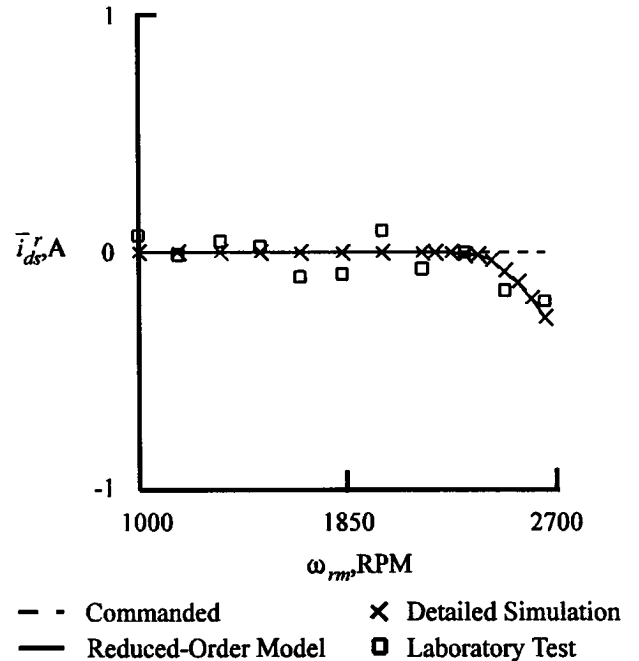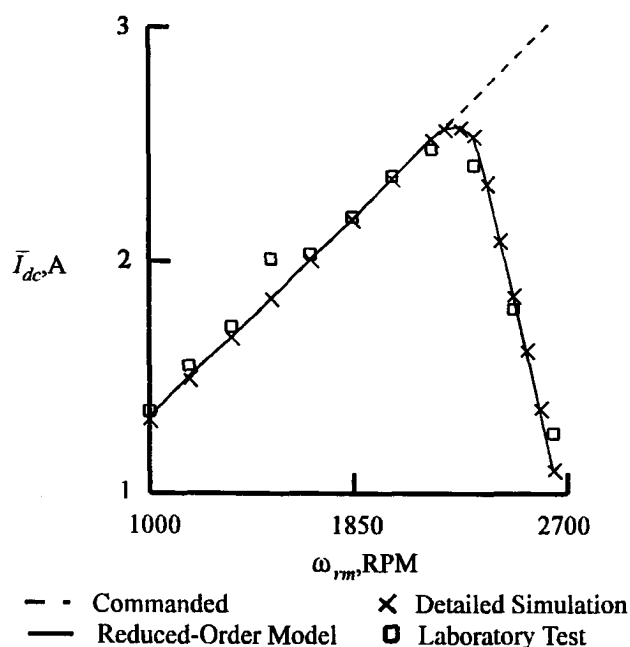

Figure 8. Average d-axis current.

Figure 9. Average dc link current.

As can be seen, there is an excellent agreement between the measured currents, the currents predicted by the detailed simulation, and the currents predicted by the reduced-order model. The discrepancy between the measured torque and that predicted by the reduced-order model and computer simulation is at least partly due to inaccuracy in the torque table in this range (the torque table is rated at 56 N•m). Comparison of the averave-value model to the detailed simulation for other machines also gives excellent agreement. For the purposes of demonstrating the utility of the model set fourth herein, a
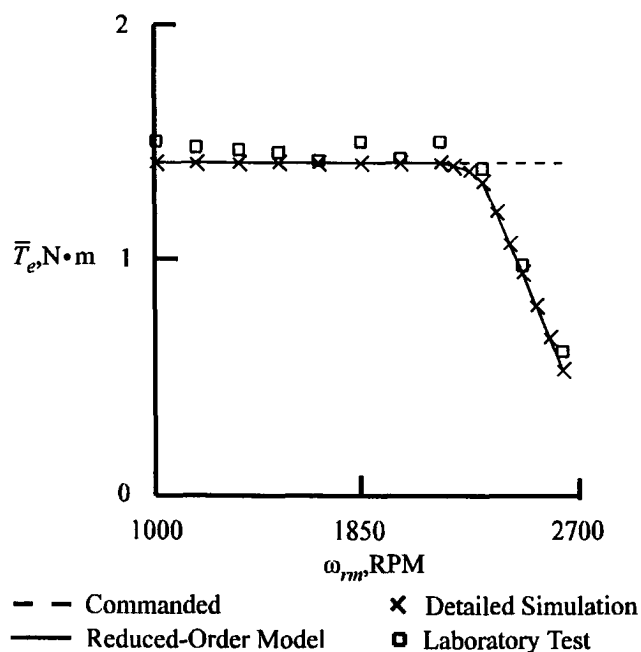

Figure 10. Average electromagnetic torque.

dynamic study was performed in which the dc voltage is set to $V_{dc} = 100$ V and the machines start-up performance is observed while applying a mechanical load torque of $T_L = 10^{-5} * \omega_{rm}^2$. During this study, all four modes of system operation were encountered. The reduced-order model based simulation was found to be over 300 times faster than the detailed computer simulation, and the predicted results were identical.

V. CONCLUSION

An average-value reduced-order model of a hysteresis current controlled brushless dc machine has been set fourth. In so doing, it was observed that the drive possesses five distinct operating modes, each of which retains a characteristic current waveform. The operating modes the drive exhibits were defined as a function of the severity of inverter saturation which occurs at high speeds due to the increase in the back emf. The reduced-order model has been verified both experimentally and using a detailed simulation, and was found to be over 300 times faster than a detailed simulation in computing electro-mechanical transients.

VI. ACKNOWLEDGMENTS

VII. REFERENCES

[1] P.C. Krause, F. Nozari, T. L. Skvarenina, and D. W. Olive, " The Theory of Neglecting Stator Transients", IEEE Transactions on Power Apparatus and Systems, Vol. PAS-98, pp 141-148, Jan./Feb. 1979.

[2] S. R. Macminn, T. M. Jahns, "Control Techniques for Improved High-Speed Performance of Interior PM Synchronous Motor Drives", IEEE Trans. on Industry Applications, Vol. IAS-27, no. 5, pp 997-1004, Sept./Oct. 1991.

[3] R. Dahouadi, N. Mohan, "Analysis of Current-Regulated Voltage-Source Inverters for Permanent Magnet Synchronous Motor Drives in Normal and Extended Speed Ranges", IEEE Transactions on Energy Conversion, Vol. EC-5, no. 1, pp137-144, March 1990.

[4] P. C. Krause, "Analysis of Electric Machinery," McGraw-Hill, 1986.

[5] T. W. Nehl, N. A. Demerdash, "Impact of Winding Inductances and other Parameters on the Design and Performance of Brushless DC Motors," IEEE Transactions on Power Apparatus and Systems, Vol. PAS-104, pp. 2206-2213, August 1985.

[6] S. D. Sudhoff, K. A. Corzine, and H. J. Hegner, "A Flux Weakening Strategy for Current-Regulated Surface-Mounted Permanent Magnet Machine Drives," accepted for publication, IEEE Transactions on Energy Conversion, 1994.

Keith A. Corzine received the BSEE and MSEE degrees from the University of Missouri - Rolla in 1992 and 1994, respectively, and is currently pursuing the Ph.D. degree. His interest include the design and modeling of electric machinery and electric drive systems.

Scott D. Sudhoff received the BSEE, MSEE, and Ph.D. degrees at Purdue University in 1988, 1989, and 1991, respectively. He is currently an Assistant Professor at the University of Missouri - Rolla. His interest include the analysis, simulation, and design of electric machinery, drive systems, and finite-inertia power systems. He has authored or co-authored nine journal papers in these areas.

Henery J. Hegner received the BSEE degree from Virginia Polytechnical Institute and State University in 1992. He is employed with the Electrical Systems Division of the Propulsion and Auxiliaries Department at the Naval Surface Warfare Center, Annapolis, Maryland. He is currently a member of the U.S. Navy's Advanced Surface Machinery Programs where he is serving as Team Leader of the DC Zonal Electrical System Program. For the past 14 years, he has specialized in electrical systems and components for Naval shipboard systems, and now has several papers in this area.